Civil Engineering and Applied Solutions

Research Article

journal homepage: ceas.journals.umz.ac.ir

CEAS Civil Engineering and Applied Solutions

Influence of Localized Beam Cracking Representation on Nonlinear Seismic Performance of RC Moment Frames

Ehsan Abbasalipour [a], Mehdi Dehestani [b*], Aref Hasanzadeh [b]

[a] *Department of Civil Engineering, Se.C., Islamic Azad University, Semnan, Iran*
[b] *Faculty of Civil Engineering, Babol Noshirvani University of Technology, Babol, Iran*

ARTICLE INFO

Article history:

Received 06 June 2026

Revised 28 June 2026

Accepted 01 August 2026

Available online 01 April 2027

Keywords:

Reinforced concrete cracking

Localized stiffness reduction

Seismic performance

Nonlinear static analysis

Nonlinear dynamic analysis

ABSTRACT

Cracking in reinforced concrete (RC) members is a key mechanism governing stiffness degradation and seismic response of structural systems. This study examines the influence of different beam-cracking modeling approaches on the nonlinear seismic behavior of RC moment-resisting frames. Three RC frames with 3, 6, and 9 stories are analyzed under three modeling schemes: (1) uncracked elastic model, (2) code-based effective stiffness reduction model, and (3) localized cracking model distributed along beam elements. In the localized formulation, stiffness degradation is defined in a position-dependent manner, allowing non-uniform reduction along the member length to better represent crack concentration in plastic hinge regions and mid-span zones. This overcomes a major limitation of conventional effective stiffness methods, which assume uniform stiffness reduction and cannot capture spatial damage distribution. Nonlinear static (pushover) and nonlinear time-history analyses are performed using Imperial Valley, Duzce, and Northridge ground motions within a nonlinear analysis framework. Results show that cracking representation significantly affects seismic response. Considering cracking reduces initial stiffness, increases fundamental period, and decreases base shear capacity. In the code-based model, base shear capacity decreases by up to 32%, while roof displacement increases by 21%, 26%, and 8% for the 3-, 6-, and 9-story frames, respectively. The localized cracking model yields responses between the uncracked and code-based models and consistently predicts lower displacements than the latter. Crack distribution also significantly influences bending moments, plastic hinge formation, and energy dissipation. Overall, the localized cracking model provides an improved representation of stiffness degradation effects and a practical simplified framework for nonlinear seismic assessment of RC frames.

How to cite this article: Abbasalipour, E., Dehestani, M., Hasanzadeh, A. Influence of Localized Beam Cracking Representation on Nonlinear Seismic Performance of RC Moment Frames. Civil Engineering and Applied Solutions. 2027; 3(2): 102–121. doi:10.22080/ceas.2026.32032.1109.

1. Introduction

The bond between concrete and reinforcing steel constitutes one of the primary mechanisms responsible for force transfer and the satisfactory performance of reinforced concrete (RC) members. Perfect bond conditions do not exist in practice, and relative slip develops between concrete and reinforcement due to strain incompatibility between the two materials. This phenomenon leads to stiffness degradation, reduced energy dissipation capacity, and alterations in the ductility characteristics of structural members. Bond behavior is generally characterized through three successive stages: initial adhesion, stress transfer through reinforcement ribs following crack formation, and eventual bond failure resulting from insufficient concrete confinement. Crack distribution and strain

* Corresponding author.
E-mail addresses: dehestani@nit.ac.ir (M. Dehestani).

https://doi.org/10.22080/ceas.2026.32032.1109
ISSN: 3092-7749/© 2027 The Author(s). Published by University of Mazandaran.

localization in RC members are governed by the interaction between concrete softening and reinforcement-induced tension stiffening, while crack spacing is influenced by energy dissipation mechanisms within the member [1].

Cracking is recognized as one of the most influential factors affecting both the stiffness and durability of RC members. Cracks may develop due to flexure, shear, torsion, concrete shrinkage, reinforcement corrosion, thermal variations, and differential settlement, thereby influencing structural performance at both serviceability and ultimate limit states [1]. Although reinforcement contributes to controlling crack propagation and improving crack distribution, the post-cracking response remains highly dependent on concrete-steel bond characteristics, confinement conditions, and the nonlinear behavior of the constituent materials.

Extensive research has been conducted on bond-slip behavior and the modeling of concrete-steel interaction. The concrete-steel interface has been represented as a bond zone in which force transfer is simulated through bond stresses and relative slip. Despite providing accurate predictions, the increased number of degrees of freedom and the associated computational complexity have limited the applicability of such approaches in large-scale structural models [2]. Experimental bond stress-slip relationships under monotonic and cyclic loading conditions have been widely employed in the analysis of RC members and connections [3], and numerical investigations have demonstrated that accurate prediction of structural response requires the simultaneous consideration of reinforcement nonlinearity and bond-slip effects [4, 5].

To reduce computational demands, several simplified modeling approaches have been proposed. Equivalent reinforcement stiffness formulations allow bond-slip effects to be incorporated without significantly increasing model degrees of freedom [6], while fiber-based formulations represent bond-slip effects through equivalent strain components within member behavior [7-10]. Bond interface elements developed within the finite element framework have demonstrated considerable capability in reproducing the hysteretic response of RC members, although at the expense of higher computational cost [11-14]. Neglecting bond-slip effects leads to an overestimation of member stiffness and an underestimation of displacement demands in RC structures [15-17]. The representation of bond-slip behavior in regions experiencing inelastic deformations, particularly within plastic hinge zones, remains a challenge for conventional models and often requires additional modifications [18, 19]. Consequently, advanced analytical models have been proposed to predict bond-slip behavior and associated failure mechanisms with greater accuracy [20].

Alongside bond modeling, considerable attention has been devoted to crack propagation and its influence on the structural behavior of RC members. Crack location and depth can substantially affect the dynamic response and natural frequencies of structural elements [21, 22], and crack propagation in heterogeneous materials may significantly alter failure paths and damage evolution patterns [23-25]. Reinforcement corrosion and associated cracking phenomena have been identified as major contributors to stiffness degradation and durability reduction [26, 27]. Explicit formulations describing strain and slip distributions along reinforcing bars, while accounting for bond degradation mechanisms, have been developed to address localized cracking behavior [28-32], and studies on nonlinear RC frame modeling have further highlighted the significant role of connection deformability in determining seismic response characteristics [33]. Cracking has been shown to contribute to reductions in dynamic stiffness, modifications of modal characteristics, and deterioration of serviceability performance in RC structures [34]. Long-term crack development accelerates stiffness degradation and increases seismic vulnerability over time [35], while pre-existing cracks may adversely affect the residual strength of structural members subjected to fire exposure [36]. The reinforcement ratio and steel fiber reinforcement have been identified as significant parameters governing member ductility and post-cracking behavior. Fracture mechanics-based approaches and fictitious crack models have been developed to predict the nonlinear behavior of cracked RC beams, offering improved representation of these phenomena [37-40].

Despite substantial progress in this field, most existing seismic assessment approaches still represent cracking effects using uniform effective stiffness reduction factors applied along the entire member length. This simplifying assumption neglects the spatially non-uniform nature of cracking in RC members, particularly under seismic loading conditions. In reality, crack formation is highly localized and tends to concentrate in regions of maximum curvature demand, such as beam-column joints and potential plastic hinge zones.

However, conventional effective stiffness methods do not explicitly capture: (I) spatial variability of cracking along the member length, (II) interaction between localized cracking and plastic hinge formation, and (III) the resulting non-uniform stiffness degradation governing nonlinear seismic response behavior. As a result, these approaches may introduce bias in the prediction of stiffness distribution, displacement demand deformation distribution, and energy dissipation capacity of RC structural systems. Although fiber-based and detailed finite element models can represent such localized effects with higher accuracy, their implementation generally requires more detailed modeling assumptions and higher computational effort, which may limit their application in large-scale parametric seismic studies.

To address this limitation, the present study proposes a localized, position-dependent beam cracking representation, in which stiffness reduction is applied non-uniformly along beam elements based on expected damage concentration zones, including plastic hinge regions and mid-span areas. Unlike conventional code-based approaches, the proposed model explicitly accounts for the spatial distribution of cracking rather than assuming uniform stiffness loss.

The novelty of this study lies in systematically investigating the influence of spatially varying cracking representation on the nonlinear seismic response of RC moment-resisting frames with different heights. The proposed formulation provides an intermediate modeling framework between simplified code-based stiffness assumptions and more detailed nonlinear modeling approaches by incorporating spatially varying stiffness degradation within conventional frame analysis procedures. From a practical standpoint, the proposed method enhances the understanding of stiffness redistribution, plastic hinge development, and energy dissipation mechanisms, thereby offering improved insight for performance-based seismic assessment of RC structures.

Accordingly, the proposed framework introduces a position-dependent stiffness degradation strategy along RC beams that captures localized cracking effects in critical regions, providing a more detailed representation of stiffness variation compared with conventional uniform stiffness reduction approaches within nonlinear seismic analysis.

2. Numerical modeling and methodology

2.1. Design and modeling of structural frames

In this study, three-, six-, and nine-story reinforced concrete (RC) moment-resisting frames with residential occupancy and regular configurations in both plan and elevation were investigated. The structures were assumed to be located in a region of high seismic hazard and founded on Type II soil, in accordance with the Fourth Edition of the Iranian standard No. 2800. Structural modeling and analyses were performed using the SAP2000 software package.

To evaluate the influence of stiffness degradation caused by beam cracking on the seismic response of RC structures, nonlinear static (pushover) and nonlinear dynamic analyses were conducted. The nonlinear dynamic analyses were performed using three near-fault ground motion records, namely Imperial Valley, Duzce, and Northridge earthquakes. The dead loads of floors and roof were taken as 550 kg/m², while the live loads of floors and roof were assumed to be 200 $\mathrm{kg/m^2}$ and 150 kg/m², respectively. A story height of 3.2 m was considered for all structures, and the lateral load-resisting system was selected as a reinforced concrete intermediate moment-resisting frame. The analytical models of the studied frames are presented in Figs. 1 to 3.

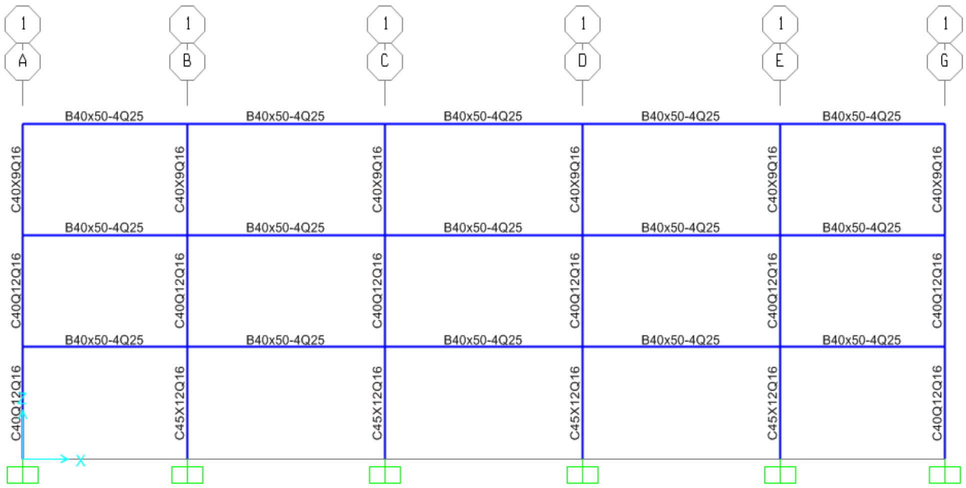

Fig. 1. Three-story intermediate reinforced concrete moment-resisting frame.

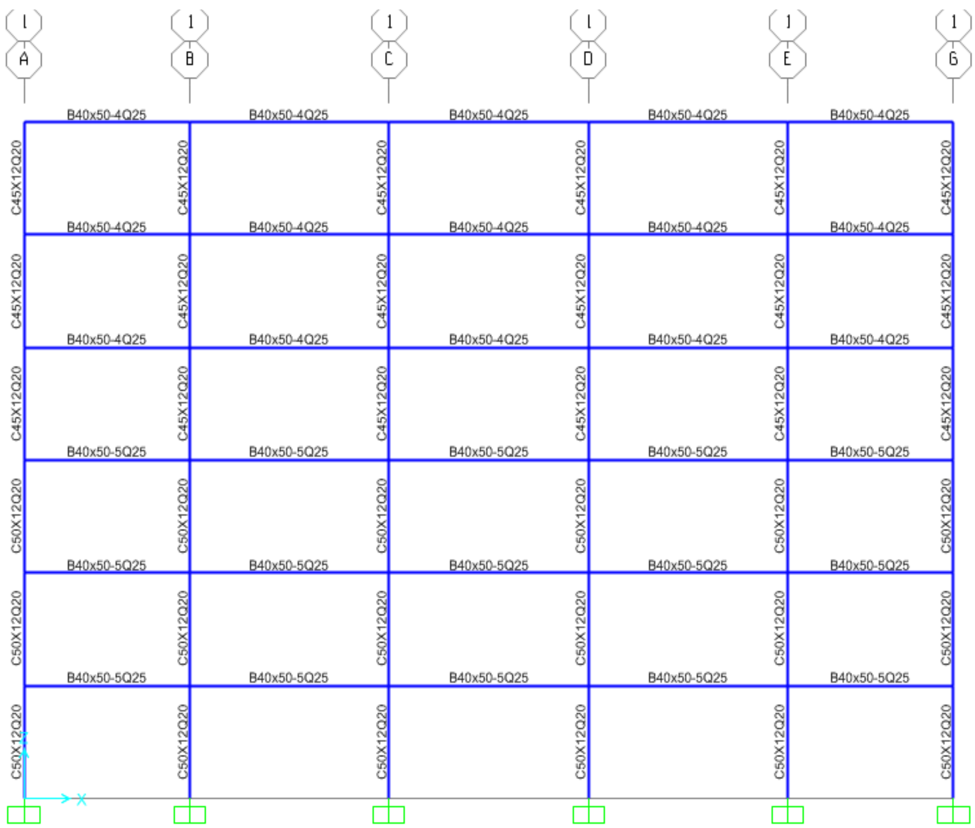

Fig. 2. Six-story intermediate reinforced concrete moment-resisting frame.

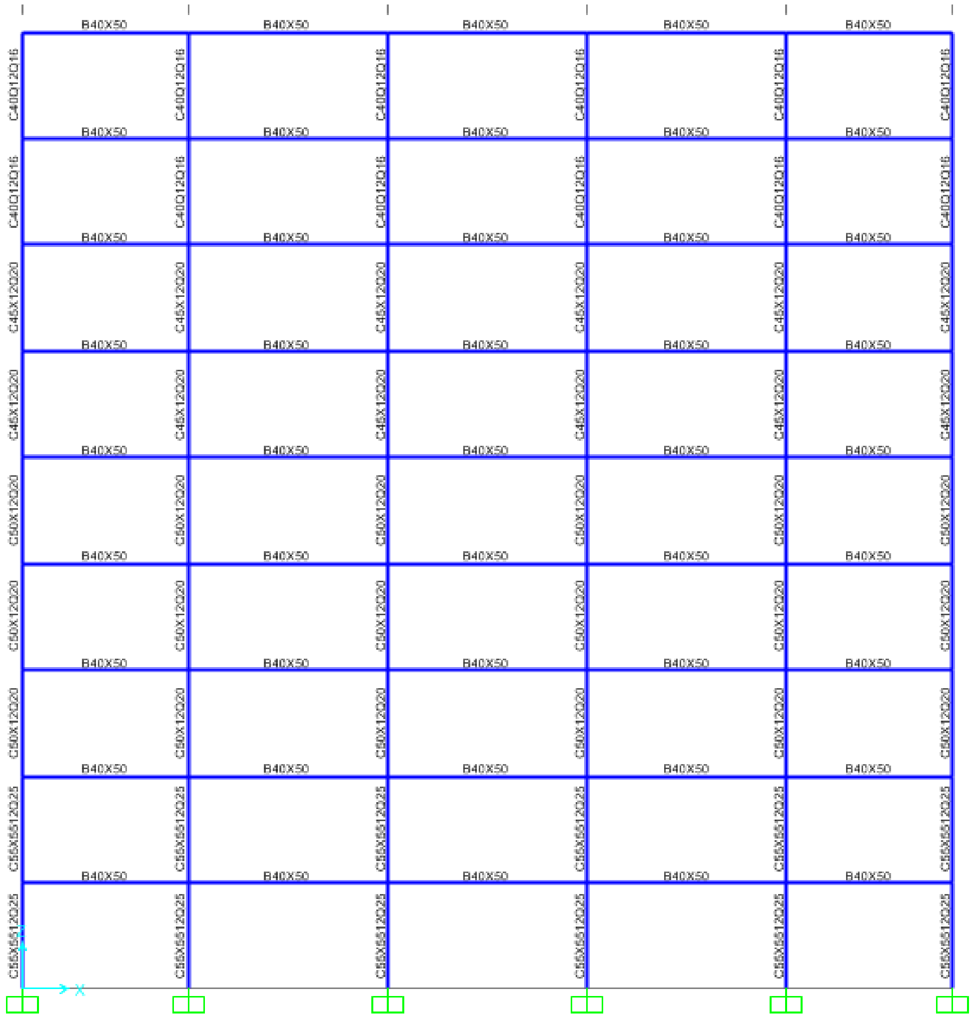

Fig. 3. Nine-story intermediate reinforced concrete moment-resisting frame.

To investigate the influence of cracking modeling approaches on the seismic behavior of the structures, three different modeling scenarios were considered: (I) an uncracked model, (II) a code-based stiffness reduction model, and (III) a localized cracking model. In the first scenario, the beam stiffness was defined without considering the effects of cracking. In the second scenario, beam stiffness was reduced according to the provisions of the Iranian standard No. 2800 by applying a stiffness modification factor of 0.35 to the flexural stiffness of beam members. In the third scenario, stiffness reduction was implemented locally in regions susceptible to crack concentration and plastic hinge formation.

Within the proposed localized cracking approach, the effective stiffness values of beam members were determined using the analytical relationships developed in the present study and subsequently assigned to critical regions of the beams, including both end zones and the mid-span region. Based on the findings reported by Forouzan [41], the stiffness degradation resulting from localized cracking and bond-related effects can be represented through an equivalent modification of the effective beam stiffness. The formulation proposed by Forouzan [41] was developed based on experimental investigations on reinforced concrete beam specimens, and its applicability was examined through comparisons with available experimental results. In this approach, the adjusted steel elastic modulus is introduced only as a numerical parameter to reproduce the experimentally supported reduction in member-level stiffness within the cracked regions of the beam model. Accordingly, the modified values were implemented within the beam elements to simulate the influence of localized deterioration effects on the global seismic response. The stiffness reduction factors employed in the analyses were calculated based on the analytical formulations proposed in this study and the reference methodology presented in Forouzan [41].

In this study, in order to account for the effect of slip in the beam-column connection region, the total beam displacement is decomposed into two components: flexural displacement, $\Delta_{bending}$, and displacement induced by connection rotational slip, Δ_{θ}. Accordingly, the total member displacement is obtained as the sum of these components, expressed as $\Delta_{total} = \Delta_{bending} + \Delta_{\theta}$.

The slip in the fixed-end region is further divided into two parts: axial slip resulting from the pull-out of embedded reinforcing bars, Δ_{axial}, and slip induced by flexural cracking in the beam end region, $\Delta_{bending}$. These two components are combined based on the principle of superposition to represent the total connection slip. The same slip-based stiffness modification framework was applied consistently across all three modeling scenarios to ensure uniform consideration of bond-slip effects.

The axial slip behavior is modeled based on the bond stress between concrete and steel along the development length of the reinforcing bars. For this purpose, analytical relationships and stress-slip models calibrated against experimental results are employed, and calibration parameters are adopted from previous studies [42]. In addition, the Gergely-Lutz empirical relationship is used to control crack width and to establish a link between cracking and slip behavior [43]. The second component of slip is associated with flexural cracking in the beam end region, where, after cracking, the tensile contribution of concrete is neglected, and force transfer is primarily carried by steel reinforcement. In this context, compatibility of strains and section equilibrium relations are used to incorporate the effect of this type of slip on the displacement response of the member. Finally, the total slip and beam displacement are implemented in the numerical model as an equivalent effect on the torsional and flexural stiffness of the member and are used in the nonlinear structural analysis.

2.2. Modification of beam stiffness due to bond slip

To incorporate the effect of end rotation in the plastic hinge region, the beam flexural stiffness (EI) is reduced within the plastic hinge length, L_P, at the member end, while the supports are modeled as fixed. In the present study, the localized cracking region is assumed to coincide with the plastic hinge zone at the beam ends, where the stiffness degradation associated with cracking and bond-slip effects is introduced. Accordingly, the length of the affected region is defined by the plastic hinge length L_P. For the determination of the plastic hinge length L_P, several empirical relationships have been proposed, among which the Sheikh and Bayrak formulation is commonly used. This expression includes parameters such as the section depth and an experimentally calibrated coefficient (ranging between 0.9 and 1.0) [44]. In the present study, an appropriate value of this coefficient is selected based on the modeling conditions. Subsequently, by equating the displacement obtained from the modified stiffness model with the displacement resulting from the rotational stiffness k_θ at the support, and employing the moment-area method, the equivalent stiffness in the plastic hinge region, EI_{eq}, is determined.

2.2.1. Evaluation of the modified stiffness in an internal continuous beam

Based on the study by Forouzan [41], in an internal continuous beam with an end rotational stiffness k_θ subjected to a uniformly distributed lateral load W, the lateral displacement consists of two components: the flexural deformation and the deformation induced by end rotation. Accordingly, the total displacement is expressed as shown in Eq. 1.

$$\Delta_1 = \frac{WL^4}{384EI} + \frac{WL^3}{48k_\theta} \tag{1}$$

The first term represents the flexural deformation of the beam, while the second term corresponds to the additional deformation due to the rotational stiffness k_θ at the beam ends. In this stage, the beam behavior is idealized as a cantilever member with an effective length of $L/2$ (Fig. 4).

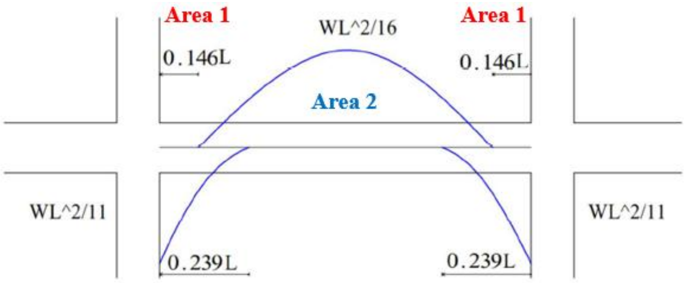

Fig. 4. Bending moment diagram of the internal continuous beam, showing the plastic hinge (localized cracking) zones at the beam ends (Area 1) and the remaining elastic region (Area 2) [41].

By equating the actual beam deflection with that of an equivalent beam having a reduced flexural rigidity EI_{eq}, and employing the moment-area method, the modified stiffness is determined. Accordingly, the bending moment distribution is evaluated considering symmetry in the two half-spans, and the moment functions are derived for two regions. Hence, the bending moment expression for Region 1 of the internal continuous beam is given by Eq. 2.

$$M_1 = -\frac{Wx^2}{2} + \frac{WLx}{2} - \frac{WL^2}{11} \tag{2}$$

The bending moment expression for Region 2 is given by Eq. 3.

$$M_2 = 0.4987Wx^2 - 0.353WLx \tag{3}$$

Boundary conditions and symmetry at the supports and midspan are then applied to determine the unknown coefficients. The deflection is evaluated using the moment-area method for half of the span only, as in Eq. 4.

$$\Delta = \int \frac{M(x)\,x}{EI}\,dx \tag{4}$$

Finally, the actual deflection is equated to the deflection of the equivalent model, as Eq. 5.

$$\Delta(EI_{eq}) = \Delta_{real} \tag{5}$$

From this equality, the equivalent flexural rigidity EI_{eq} is obtained as Eq. 6.

$$\frac{1}{EI_{eq}} = \frac{1}{EI} + \frac{1}{24\beta k_\theta L} \tag{6}$$

where $\beta = (-0.2495\alpha^3 + 0.201\alpha^2 - 0.004495\alpha)$ and $\alpha = L_P/L$. The coefficient β represents the position-dependent stiffness modification function used to describe the stiffness variation within the localized cracking region. Therefore, the stiffness reduction is not uniformly distributed along the beam length but is governed by the normalized cracked length parameter.

2.2.2. Evaluation of the modified stiffness in an exterior continuous beam

The moment distribution in an exterior continuous beam is not symmetric (Fig. 5); therefore, the rotations at the two supports are not identical. The maximum bending moment and maximum deflection occur at a distance of approximately $0.518L$ along the span. By dividing the beam into two segments, the exterior continuous beam can be idealized as two cantilever-type members with fixed-fixed-free boundary conditions, having lengths of $0.518L$ and $0.482L$, respectively. Each fixed-fixed-free beam segment with length L is equivalent to a fixed-fixed beam with an effective length of $2L$ [41].

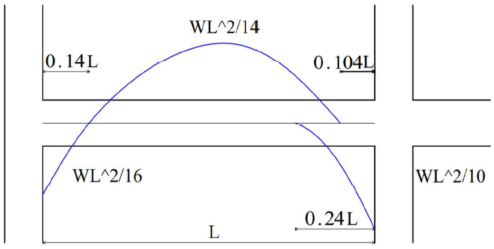

Fig. 5. Bending moment diagram of the exterior continuous beam [41].

2.2.3. Modified stiffness at 0.518L

The bending moment diagram of a fixed-fixed beam with a total length of $1.036L$ is shown in Fig. 6.

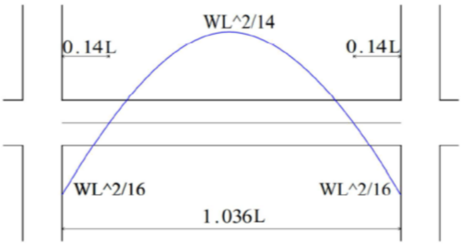

Fig. 6. Bending moment diagram of a fixed-fixed beam with a length of $1.036L$ in the exterior continuous beam [41].

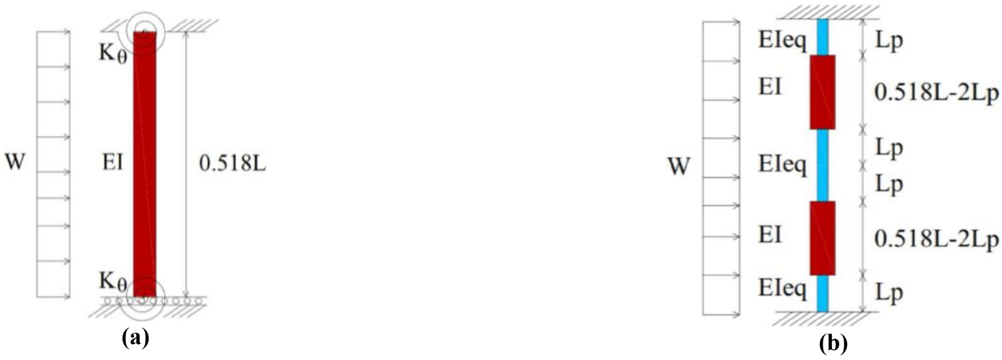

Fig. 7. (a) Simplified model of a fixed-free beam segment with length $0.518L$ subjected to a uniformly distributed load; and (b) equivalent fixed-fixed beam model with length $1.036L$ using EI_{eq} [41].

If a beam with rotational stiffness $k_{\theta 1}$ at both ends is subjected to a uniformly distributed horizontal load W, the horizontal displacement of the model shown in Fig. 7a is given as Eq. 7.

$$\Delta_1 = 0.002999\frac{WL^4}{EI_1} + 0.0347\frac{WL^3}{k_{\theta 1}} \tag{7}$$

where the first term represents the flexural deformation of the beam and the second term corresponds to the deformation induced by the end rotational stiffness $k_{\theta 1}$.

When the same load is applied to an equivalent beam with reduced flexural rigidity EI_{eq} (Fig. 7b), the horizontal displacement is obtained using the moment-area method. The bending moment function is assumed in the form $M = ax^2 + bx + c$, and the coefficients a, b, and c are determined by applying the boundary conditions. Consequently, the bending moment equation for the fixed-fixed beam under uniform loading is expressed as Eq. 8.

$$M = -0.4913Wx^2 + 0.517WLx - \frac{WL^2}{16} \tag{8}$$

After applying the boundary conditions, the coefficients are obtained. The deflection is then computed using the moment-area integration and equated to the response of the reduced-stiffness model as shown in Eq. 9.

$$\Delta(EI_{eq}) = \Delta_{real} \tag{9}$$

Accordingly, the modified stiffness EI_{eq} at $0.518L$ is obtained as shown in Eq 10.

$$\frac{1}{EI_{1eq}} = \frac{1}{EI_1} + \frac{0.01506}{\beta_1 k_\theta L} \tag{10}$$

where $\beta_1 = (0.1663\alpha_1^3 - 0.1878\alpha_1^2 + 0.02913\alpha_1)$ and $\alpha_1 = \frac{L_P}{1.036L}$.

2.2.4. Modified Stiffness at 0.482L

The bending moment diagram of a fixed-fixed beam with a length of $0.964L$ is presented in Fig. 8 [41].

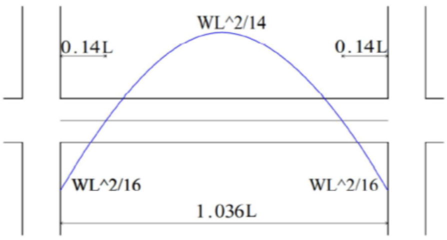

Fig. 8. Bending moment diagram of a fixed-fixed beam with a length of $0.964L$ in the side continuous beam [41].

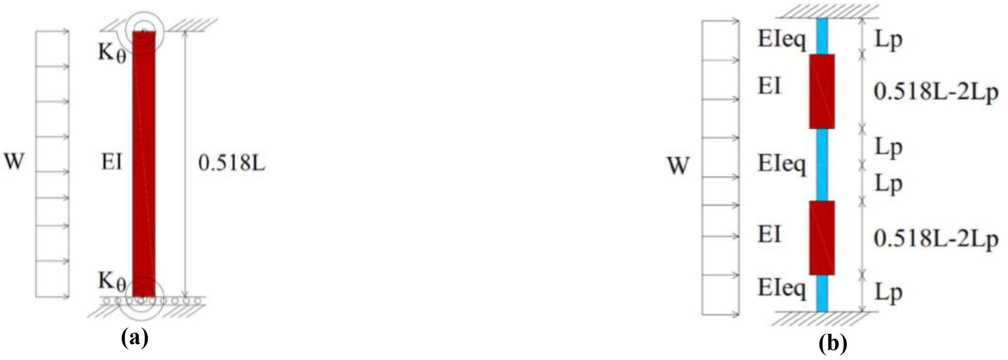

Fig. 9. (a) Simplified model of a fixed-roller beam with a length of $0.482L$ subjected to a uniformly distributed load; and (b) simplified model of a fixed-fixed beam with a length of $0.964L$ subjected to a uniformly distributed load [41].

When a beam with rotational stiffness at both ends is subjected to a uniformly distributed horizontal load W, as shown in Fig. 9a, the horizontal displacement is given by Eq. 11.

$$\Delta_1 = 0.00225\frac{WL^4}{EI_2} + 0.01866\frac{WL^3}{k_{\theta 2}} \tag{11}$$

The first term represents the flexural deformation of the beam, while the second term corresponds to the deformation associated with the rotational stiffness at the beam ends. When an equivalent load is applied to the beam with reduced stiffness EI_{eq} at both ends (Fig. 9b), the horizontal displacement is determined using the moment-area method. The bending moment diagram of the fixed-fixed beam with a length of $0.964L$ is divided into two segments. In each segment, the bending moment equation is expressed in the form $M = ax^2 + bx + c$, where the coefficients a, b, and $c$are obtained by applying the boundary conditions. The moment equation for the first region of the side continuous beam is expressed as Eq. 12.

$$M = -0.5722Wx^2 + 0.5516WLx - \frac{WL^2}{10} \tag{12}$$

The moment equation for the second region of the side continuous beam is given by Eq. 13.

$$M = 0.291Wx^2 - 0.2205Wx \tag{13}$$

Using symmetry, the analysis is performed for half of the beam, and the integration domain is divided into several segments. The displacement is obtained from the moment-area method and equated to that of the equivalent model as shown in Eq. 14.

$$\Delta(EI_{eq}) = \int M(x)\,x\,dx \tag{14}$$

Consequently, the modified stiffness EI_{eq} at $0.482L$ is obtained, as shown in Eq. 15.

$$\frac{1}{EI_{2eq}} = \frac{1+0.003095/\beta_2}{EI_2} + \frac{0.01041}{\beta_2 k_{\theta 2} L} \tag{15}$$

where $\beta_2 = (0.21595\alpha_2^4 - 0.2861\alpha_2^3 + 0.1094\alpha_2^2 + 0.1242\alpha_2)$ and $\alpha_2 = \frac{L_P}{0.964L}$.

2.2.5. Relationship between the stiffness of fixed-fixed beam sections at 0.518L and 0.482L

According to the study by Forouzan [41], the formulations used in the present research have been derived and verified. In the side continuous beam, the stiffness on the two sides of the support is not identical. Assuming identical beam geometry along the span, this stiffness difference arises from variations in the amount of reinforcing steel. In addition, the displacement at the $0.518L$ region is simultaneously influenced by both flexural deformation and rotational (torsional) deformation at the supports. Therefore, by having the properties of one span, the characteristics of the opposite side (including the amount of tensile and compressive reinforcement) can be determined through an iterative trial-and-error procedure.

2.3. Calculation of $E_{s,eq}$ based on the modified stiffness

In this study, the flexural stiffness of the beam is defined as the slope of the moment-curvature diagram. Based on equilibrium considerations and assuming yielding of the tensile steel, in the sectional analysis of the beam, the difference between tensile steel forces and the compressive forces contributed by concrete and reinforcing steel is evaluated by varying the neutral axis depth. This iteration is continued until the force imbalance becomes negligible. Once the neutral axis depth is determined, the yielding of the tensile reinforcement is verified. If yielding does not occur, the trial-and-error process is repeated until tensile yielding is achieved. After determining the neutral axis depth, the bending moment capacity is calculated. The stiffness is defined based on the relationship between moment and curvature and can be expressed as Eq. 16 [41].

$$EI = A_s E_s j d^2 (1-k) \tag{16}$$

where A_s is the area of tensile reinforcement, E_s represents the elastic modulus parameter associated with the tensile reinforcement contribution in the section stiffness formulation, $k = [(\rho+\rho')(\eta)^2 + 2(\rho+\rho' \, d'/d)\eta]^{1/2} - (\rho+\rho')\eta$ and ρ is the ratio of tensile reinforcement area to concrete area, $\rho'$is the ratio of compressive reinforcement area to concrete area, and η is the ratio of the modulus of elasticity of steel to that of concrete. According to Eq. (16), the reinforcement-related parameters have a significant influence on the calculated flexural stiffness of reinforced concrete beams, whereas changes in reinforcement area alone may not provide the required stiffness modification. Whereas changes in A_s do not lead to the desired reduction in stiffness. Therefore, instead of directly modifying the constitutive behavior of reinforcing steel, an equivalent adjustment of the effective steel modulus is adopted to incorporate the stiffness degradation effect associated with cracking and bond-related effects, which consequently affects the parameters η and k. Using Eq. 16 together with the previously derived $EI_{eq}$for each beam, the equivalent steel modulus $E_{s,eq}$ is obtained [41]. It should be noted that the obtained equivalent modulus $E_{s,eq}$ is considered as a modeling parameter to represent the reduced effective stiffness of the cracked beam section rather than the actual mechanical property of reinforcing steel. For implementation in the numerical model, the calculated equivalent steel modulus $E_{s,eq}$ is assigned to the reinforcement material properties of the corresponding beam regions. Therefore, the proposed approach modifies the effective stiffness of the cracked beam segments while preserving the original constitutive behavior of reinforcing steel.

2.4. Selection and scaling of ground motion records

Near-fault ground motions exhibit distinct dynamic characteristics compared to far-field records due to the presence of velocity pulses induced by forward directivity effects and permanent displacement components. These features lead to a concentration of energy within a short time duration and can significantly amplify the nonlinear response of structures. Accordingly, the use of near-fault records is essential for a realistic assessment of seismic structural performance. In this study, three near-fault ground motions, namely Imperial Valley (1979), Northridge (1994), and Duzce (1999), were selected from the PEER database [45] to provide a consistent basis for comparative evaluation of the investigated modeling approaches. The selection was performed considering seismic characteristics such as magnitude, fault distance, faulting mechanism, and the compatibility of site conditions. The general characteristics of the selected records are presented in Table 1.

Table 1. Characteristics of selected near-fault ground motion records [45].

Record name	Event year	Location	Station	Magnitude	Fault mechanism
DUZCE	1999	Duzce, Turkey	IRIGM 487	7.14	Strike-slip
IMPERIAL VALLEY	1979	Imperial Valley	SAHOP CASA FLORES	6.53	Strike-slip
NORTHRIDGE	1994	Northridge	Pacoima Dam	6.69	Reverse

For dynamic analysis, pairs of horizontal components of the ground motions were employed. The scaling procedure was carried out in accordance with the provisions of Iranian standard 2800 as follows. First, each record was normalized such that its peak ground acceleration was equal to gravitational acceleration, g. Subsequently, the response spectra of each component were computed for 5% damping, and the combined spectrum of each pair was obtained using the square root of the sum of squares (SRSS) method. Next, scaling factors were determined such that the average of the combined spectra over the period range $0.2T$ to $1.5T$ (where T is the fundamental period of the structure) was not less than 90% of the design spectrum of standard 2800. The final scaling factors were applied to the normalized ground motions and used in nonlinear dynamic analyses. When a sufficient number of appropriate records is not available, the use of simulated ground motions compatible with the target seismic conditions is permitted. Moreover, the selected records should, as far as possible, be representative of the project site in terms of geological, tectonic, and soil conditions. The duration of strong motion is also considered to be at least 10 seconds or three times the fundamental period of the structure, whichever is greater. Finally, three pairs of scaled ground motions, in accordance with standard 2800, were used for comparative nonlinear dynamic analyses of the studied structures (3-, 6-, and 9-story buildings). The scaling results of the selected ground motions are illustrated in Figs. 10 to 12.

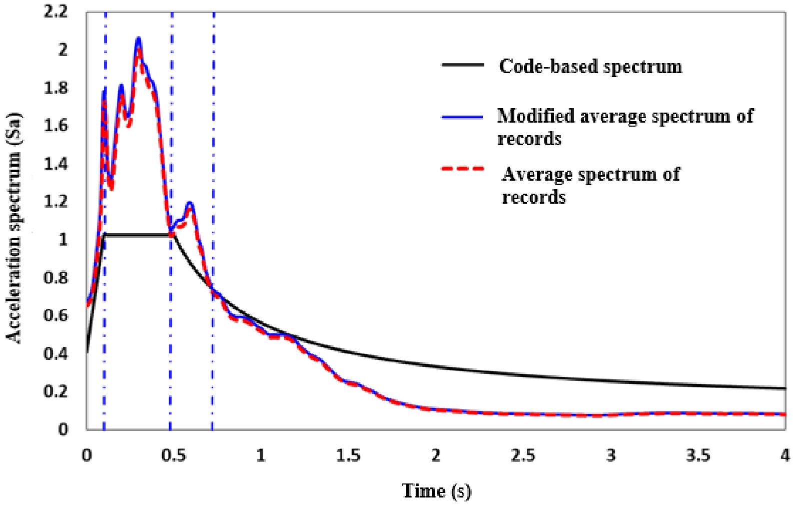

Fig. 10. Scaling of ground motions to the standard 2800 response spectrum for the 3-story structure.

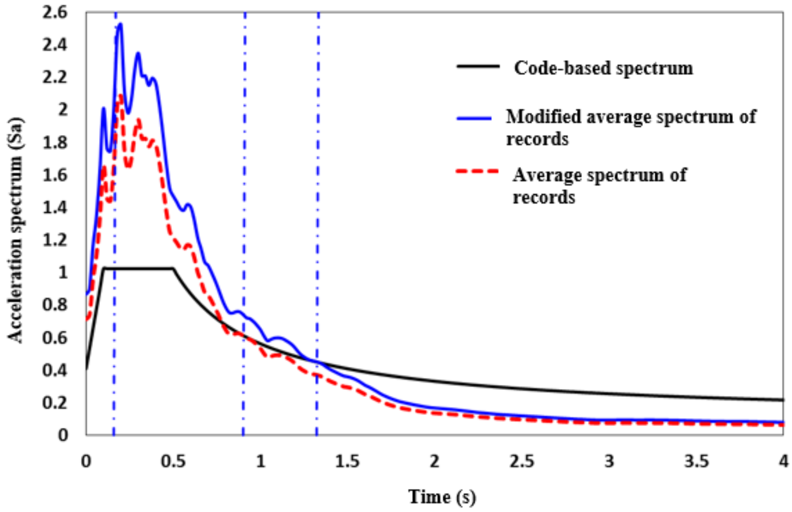

Fig. 11. Scaling of ground motions to the standard 2800 response spectrum for the 6-story structure.

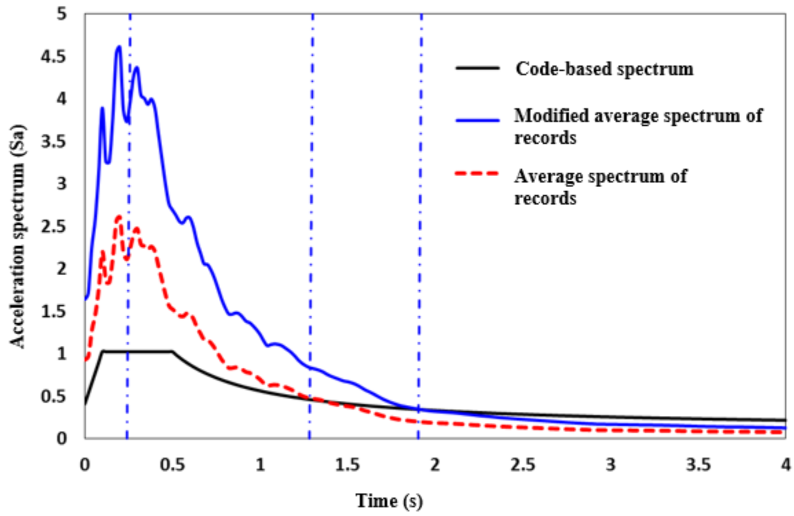

Fig. 12. Scaling of ground motions to the standard 2800 response spectrum for the 9-story structure.

The proposed localized cracking model is computationally efficient as it is implemented within the standard beam element formulation in SAP2000 without requiring mesh refinement or additional degrees of freedom. Compared with conventional detailed nonlinear modeling strategies, the proposed approach avoids the need for additional modeling complexity such as refined section discretization or increased degrees of freedom, while providing a more detailed representation of stiffness degradation than conventional uniform code-based assumptions. This makes the model suitable for practical seismic assessment of reinforced concrete moment-resisting frames.

3. Results and discussion

3.1. Static analysis results

The pushover curves for the 3-, 6-, and 9-story structures (Figs. 13 to 15) indicate that considering the cracking effect in the modeling leads to a noticeable reduction in the ultimate shear capacity and an overall degradation of the capacity curves across all investigated cases. This behavior reflects a reduction in the effective lateral stiffness of the system due to cracking. Examination of the initial slope of the pushover curves, which represents the initial stiffness of the structure, shows that the code-based cracking assumption results in a significantly more pronounced stiffness reduction, with a considerable change in the initial slope compared to the other modeling cases. This directly leads to an increase in the natural period of the structure. In contrast, in the beam-length cracking model, stiffness variations are more limited, although a reduction in the ultimate capacity is still observed.

Overall, the obtained results indicate that the cracking effect, particularly under code-based assumptions, plays a decisive role in reducing the lateral stiffness and seismic capacity of the investigated structures. Neglecting this effect may therefore lead to an unconservative estimation of the nonlinear structural response.

This behavior can be attributed to the reduction in effective flexural rigidity in cracked beam regions, which leads to a decrease in the global lateral stiffness of the structural system. In the code-based approach, the uniform stiffness reduction accelerates global softening, resulting in a more pronounced increase in the fundamental period. In contrast, the localized cracking model preserves stiffness in less damaged regions, leading to a more gradual degradation of stiffness and a smoother capacity curve response.

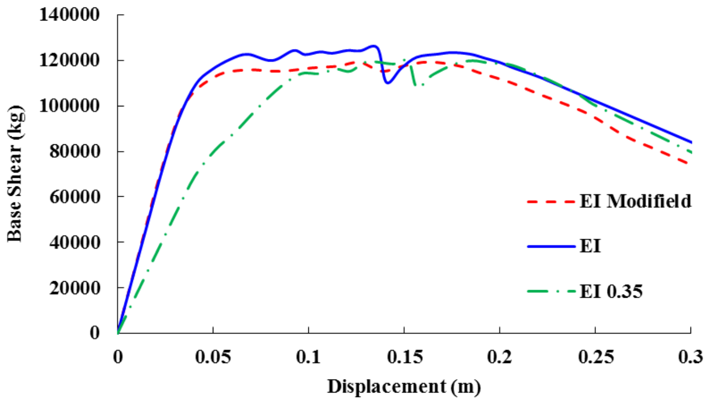

Fig. 13. Pushover curve of the 3-story structure under all three cracking assumptions.

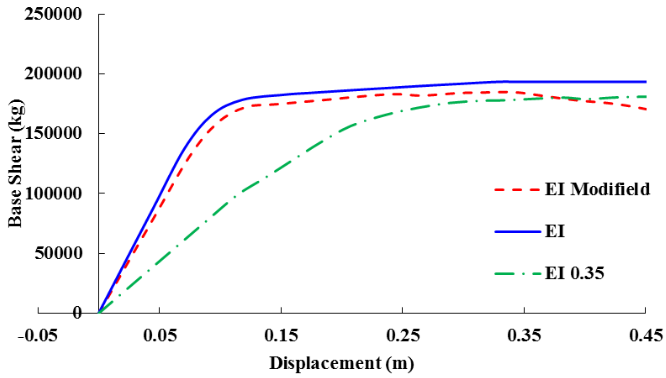

Fig. 14. Pushover curve of the 6-story structure under all three cracking assumptions.

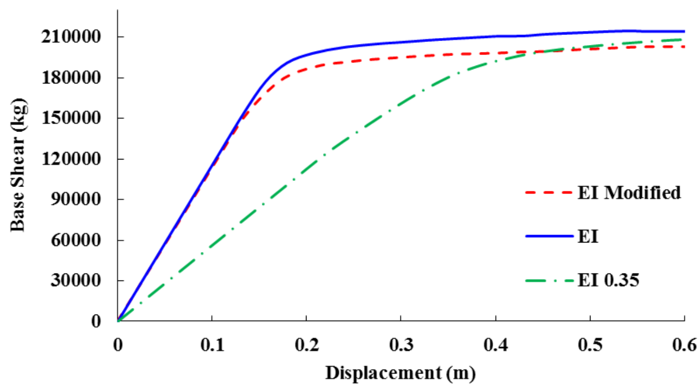

Fig. 15. Pushover curve of the 9-story structure under all three cracking assumptions.

3.2. Comparison of the effect of considering cracking in nonlinear dynamic analysis

For the 3-story structure, the inclusion of cracking had a significant influence on the seismic response under different ground motion records. In the code-based cracking model, the base shear decreased by approximately 35% based on the average response of the investigated ground motions, while the roof displacement increased by about 21% compared with the uncracked case. This reduction in base shear is primarily due to global stiffness degradation, which modifies the dynamic characteristics of the structure and reduces lateral force demand. Conversely, in the localized cracking model, stiffness degradation is distributed along beam elements rather than being uniformly applied, resulting in a more balanced redistribution of internal forces and reducing excessive global softening within the investigated cases.

The increase in roof displacement is associated with the formation of softened hinge regions at beam ends, where localized cracking significantly reduces rotational stiffness. This localized flexibility increases global deformation demand without substantially altering the overall force path of the structure. This behavior is also consistent with the formation of plastic hinge regions at beam ends, where nonlinear deformations become concentrated. The development and progression of these hinges contribute to the observed increase in global flexibility and roof displacement.

In contrast, in the beam-length cracking model, the base shear increased by approximately 10%, whereas the roof displacement remained nearly unchanged compared to the uncracked case. In terms of flexural response, the mid-span beam moment decreased by approximately 77% in the code-based cracking model, whereas an increase of about 45% was observed in the beam-length cracking model. This variation in beam moment response reflects changes in internal force redistribution mechanisms. In the code-based model, stiffness degradation reduces moment demand through global force redistribution, whereas in the localized cracking model, partial stiffness retention in beam spans allows higher moment demand to develop, particularly in mid-span regions.

Furthermore, the energy dissipation results indicate that cracking generally leads to a reduction in dissipated energy. On average, the amount of absorbed energy in the code-based cracking case was approximately 34% lower than that of the beam-length cracking model. This reduction in dissipated energy suggests a tendency toward a more concentrated inelastic response within the investigated cases, whereas the localized cracking approach promotes a more progressive development of inelastic mechanisms along beam elements, resulting in a more distributed energy dissipation pattern.

The corresponding results are illustrated in Figs. 16 to 19.

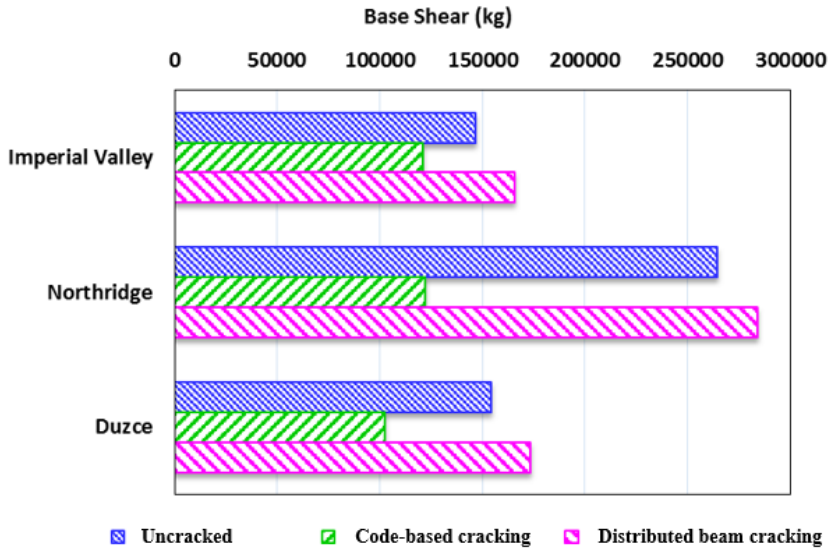

Fig. 16. Comparison of base shear responses for the 3-story structure with and without considering cracking under all ground motions.

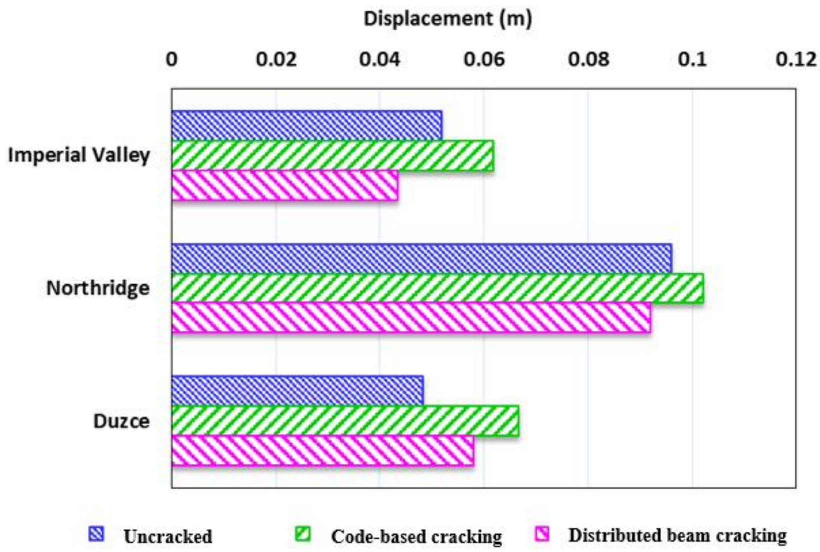

Fig. 17. Comparison of roof displacement responses for the 3-story structure with and without considering cracking under all ground motions.

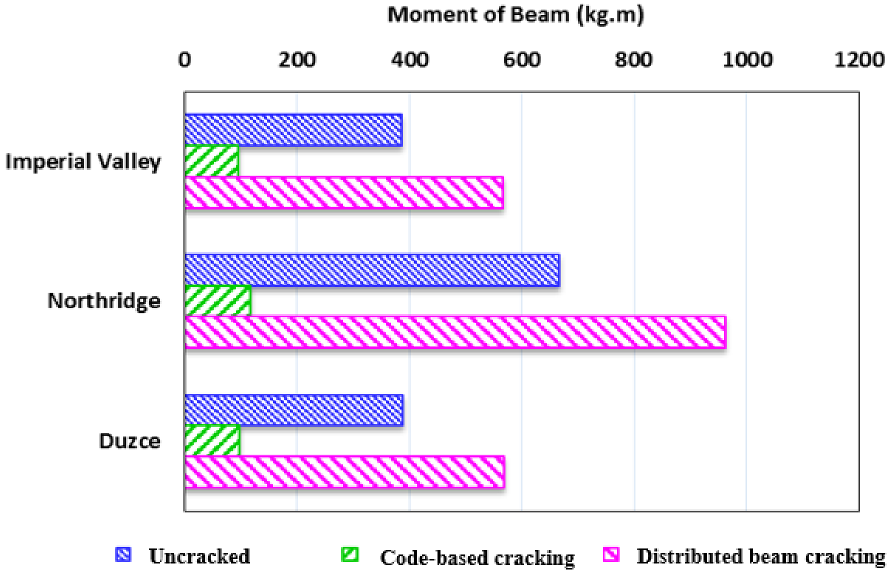

Fig. 18. Comparison of beam bending moment responses for the 3-story structure with and without considering cracking under all ground motions.

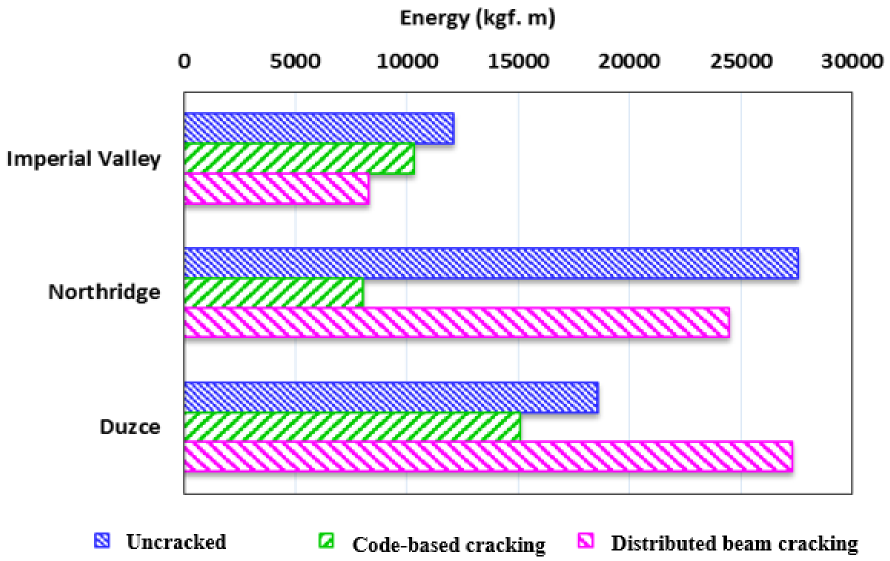

Fig. 19. Comparison of dissipated energy for the 3-story structure with and without considering cracking under all ground motions.

In the 6-story structure, consideration of cracking has led to significant variations in seismic response under different ground motion records. In the code-based cracking model, the base shear decreased by approximately 32% on average among the investigated ground motions, whereas in the beam-distributed cracking model, this reduction is about 9%. This trend is associated with increased global flexibility due to stiffness degradation, which alters the modal properties of the structure and reduces lateral force demand. In addition, the change in stiffness distribution leads to modifications in modal participation factors, where higher vibration modes become more active, resulting in a more distributed inertia force pattern along the height of the structure. However, the distributed cracking model mitigates excessive stiffness loss by preserving stiffness continuity along beam spans, leading to a more balanced global response.

Regarding roof displacement, the code-based cracking scenario resulted in an increase of approximately 26%, while in the beam-distributed cracking model, the roof displacement decreased by about 14% on average. This variation is governed by the development of localized flexibility zones in beam-end regions, which act as rotational hinges and increase the global lateral deformation response without significantly altering the global force transfer mechanism.

In terms of flexural response, the mid-span beam moment decreased by approximately 81% in the code-based cracking model and by about 16% in the beam-distributed cracking model. This significant reduction in bending moment is directly linked to the redistribution of internal forces caused by stiffness degradation, which shifts demand away from beam mid-spans toward alternative load paths within the structural system. This redistribution is governed by the progressive development of plastic hinges at beam-column connections, which serve as primary inelastic zones controlling the global response.

Furthermore, energy-related results indicate that, for most ground motion records, the dissipated energy in the code-based cracking case is, on average, approximately 19% lower than that in the beam-distributed cracking case. This reduction in dissipated energy suggests a more concentrated inelastic response in the code-based model, whereas the distributed cracking approach enables a more progressive and spatially distributed development of inelastic mechanisms along beam elements.

The corresponding results are illustrated in Figs. 20 to 23.

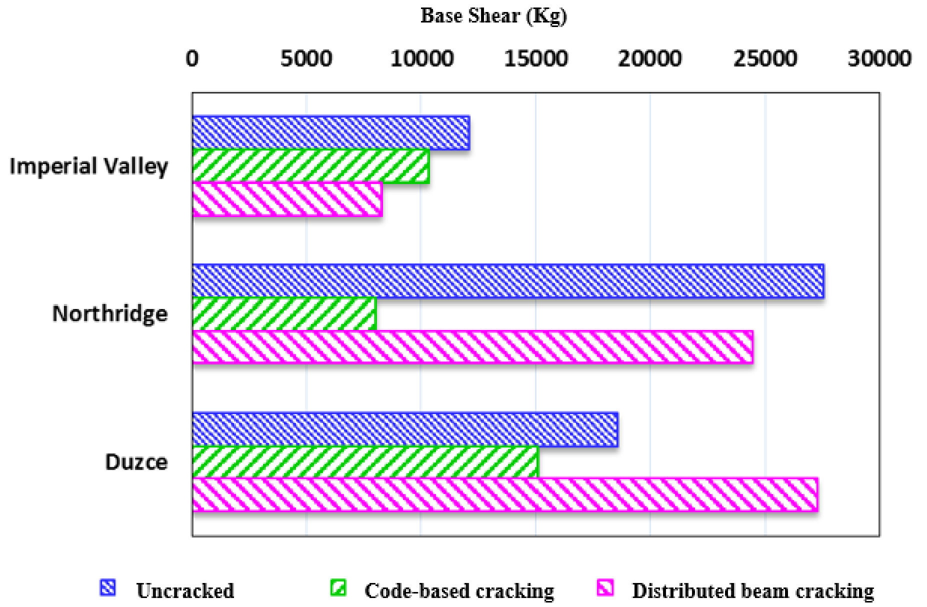

Fig. 20. Comparison of base shear results in the 6-story structure with and without considering cracking for all ground motions.

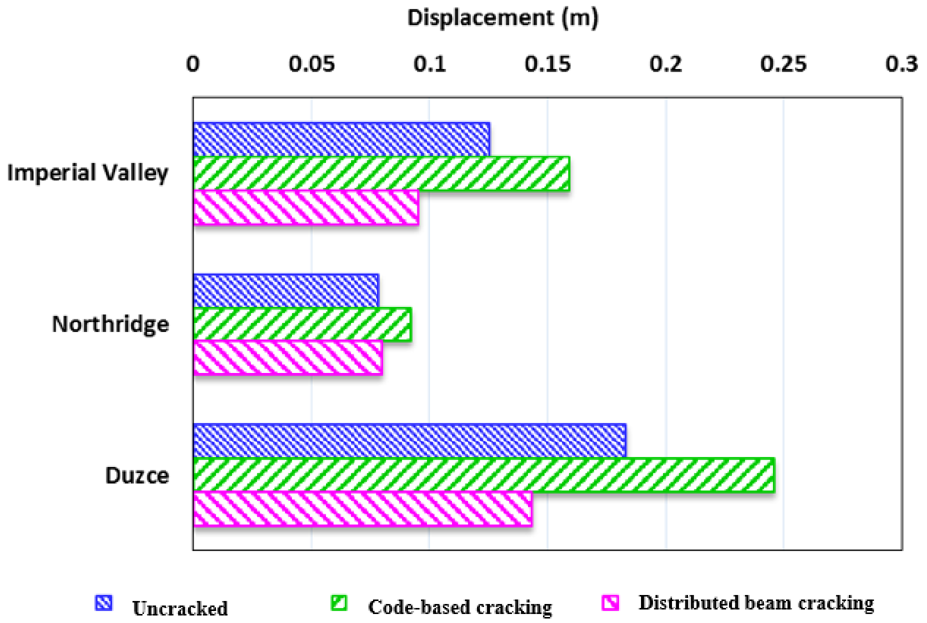

Fig. 21. Comparison of roof displacement results in the 6-story structure with and without considering cracking for all ground motions.

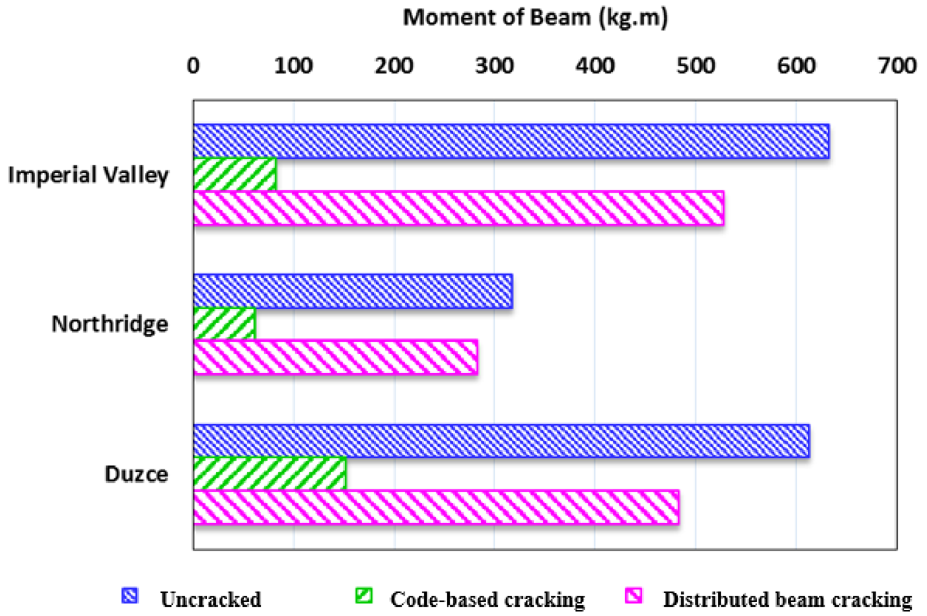

Fig. 22. Comparison of beam bending moment results in the 6-story structure with and without considering cracking for all ground motions.

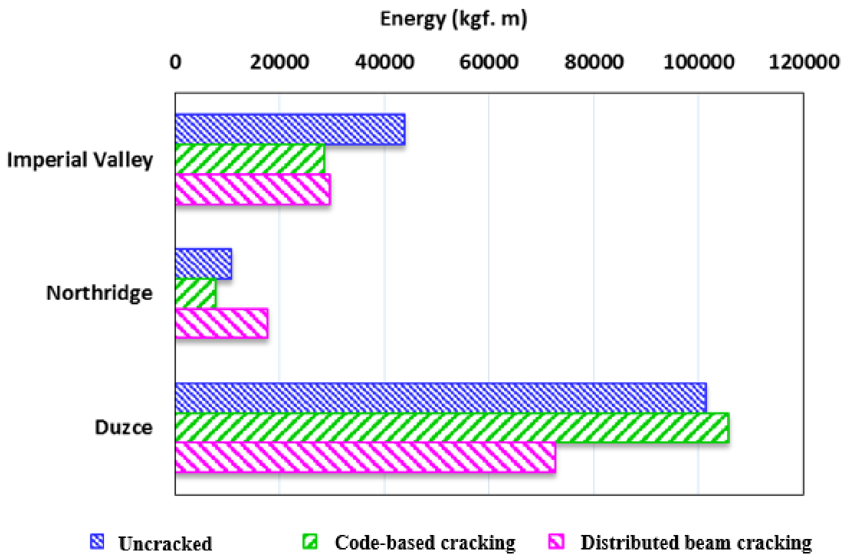

Fig. 23. Comparison of dissipated energy results in the 6-story structure with and without considering cracking for all ground motions.

In the 9-story structure, the consideration of cracking has resulted in different variations in seismic response under various ground motion records. In the code-based cracking model, the base shear decreased by approximately 31% on average among the investigated ground motions, whereas in the beam-distributed cracking model, a negligible change (approximately 1% increase) was observed compared to the uncracked case. In taller structures, the influence of higher vibration modes becomes more pronounced, which reduces the sensitivity of global response to localized stiffness changes. This increased contribution of higher modes reduces the dominance of the first mode and results in a more complex dynamic response, where stiffness changes at local levels have a reduced influence on global behavior. As a result, stiffness degradation effects are partially distributed across multiple stories rather than being concentrated in specific regions.

Regarding roof displacement, the code-based cracking model exhibited an increase of about 8%, while the beam-distributed cracking model showed an increase of approximately 5% relative to the uncracked condition. The relatively smaller increase in roof displacement compared to lower-rise structures is attributed to the higher contribution of higher vibration modes and the more distributed deformation pattern along the height of the structure, which limits the concentration of lateral deformations in specific stories.

In terms of flexural response, the mid-span beam moment decreased by approximately 81% in the code-based cracking model, whereas in the beam-distributed cracking model, an increase of about 5% was reported. This variation in bending moment response reflects a shift in internal force distribution mechanisms, where increased modal participation in taller structures leads to a more distributed demand pattern and reduces the dominance of local stiffness degradation effects.

Furthermore, energy-related results indicate that the dissipated energy in the code-based cracking case is, on average, approximately 47% lower than that in the beam-distributed cracking model. This lower sensitivity of energy dissipation suggests that in taller buildings, inelastic demands are more widely distributed across multiple stories, reducing the impact of localized cracking on global energy absorption capacity within the investigated cases.

These results are presented in Figs. 24 to 27.

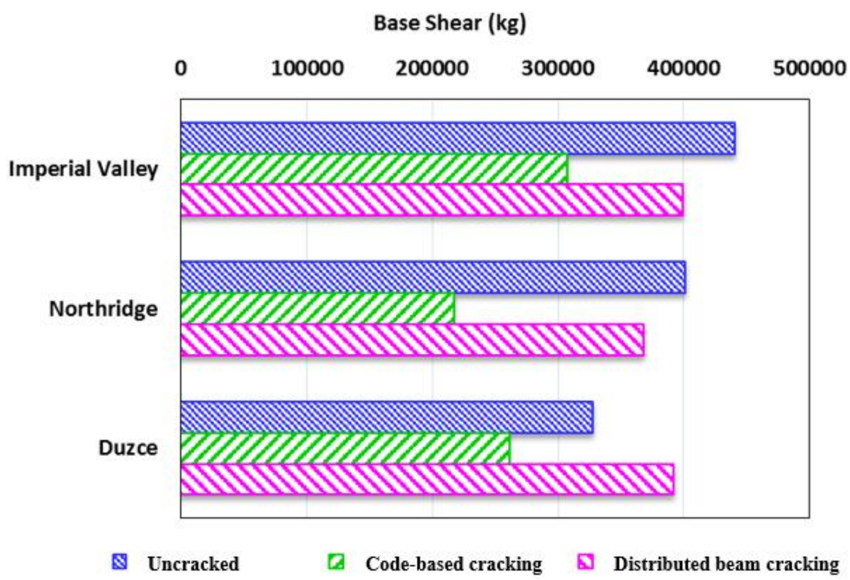

Fig. 24. Comparison of base shear results in the 9-story structure with and without considering cracking for all ground motions.

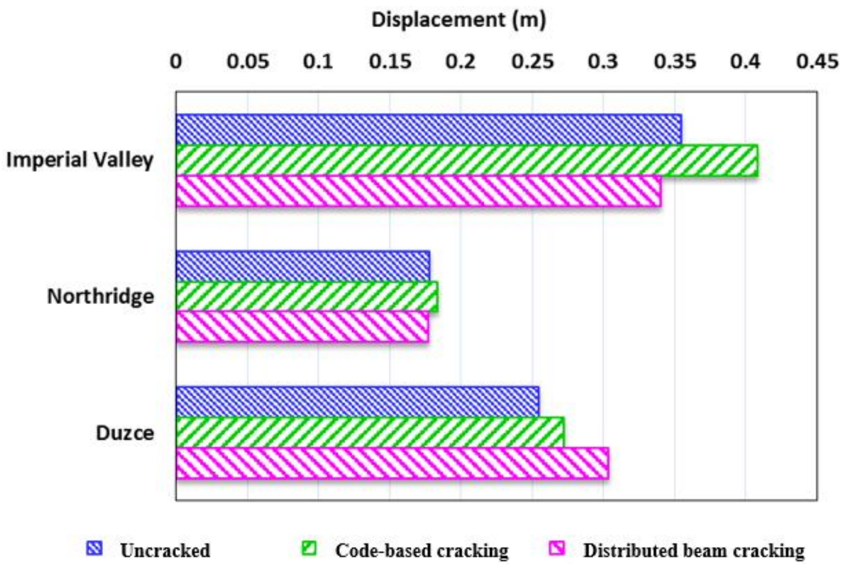

Fig. 25. Comparison of roof displacement results in the 9-story structure with and without considering cracking for all ground motions.

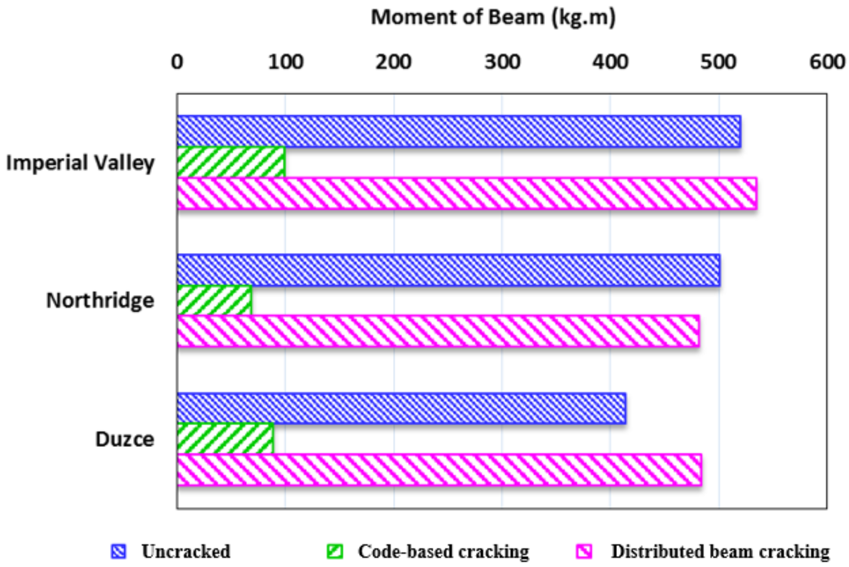

Fig. 26. Comparison of beam bending moment results in the 9-story structure with and without considering cracking for all ground motions.

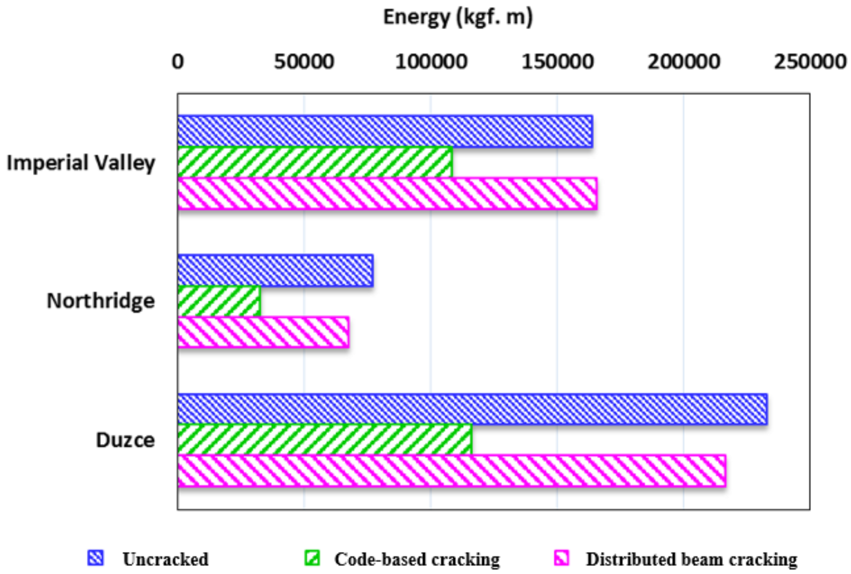

Fig. 27. Comparison of dissipated energy results in the 9-story structure with and without considering cracking for all ground motions.

To facilitate comparison among the investigated frame heights and cracking modeling approaches, Table 2 summarizes the average percentage variation of the principal response parameters relative to the uncracked model. Positive values indicate an increase, whereas negative values indicate a decrease in the corresponding response parameter.

Table 2. Summary of average percentage variations in seismic response parameters relative to the uncracked model.

Frame height	Cracking model	Base shear (%)	Roof displacement (%)	Mid-span beam moment (%)	Dissipated energy
3-Story	Code-based cracking	-35	21	-77	34% lower than beam-length cracking model
3-Story	Beam-length cracking	10	0	45	Reference
6-Story	Code-based cracking	-32	26	-81	19% lower than beam-length cracking model
6-Story	Beam-length cracking	-9	-14	-16	Reference
9-Story	Code-based cracking	-31	8	-81	47% lower than beam-length cracking model
9-Story	Beam-length cracking	1	5	5	Reference

Although interstory drift and residual deformation were not explicitly evaluated, the observed variations in roof displacement, energy dissipation, and stiffness degradation can be considered as representative indicators of global deformation demand and overall nonlinear seismic behavior. These response parameters provide a consistent basis for comparative evaluation of the investigated modeling approaches. However, these results are interpreted as comparative indicators for the considered ground motion records rather than statistically generalized seismic demand estimates. The limited number of records considered in this study did not allow a comprehensive statistical evaluation based on standard deviation, coefficient of variation, and confidence intervals.

It should also be noted that the proposed approach was not directly compared with fiber-based models in the present study. Therefore, further investigations involving experimentally validated fiber-section models are recommended to assess the accuracy and computational efficiency of the proposed modeling strategy.

4. Conclusions

In this study, the seismic response of 3-, 6-, and 9-story reinforced concrete moment-resisting frames was investigated considering different cracking representations, including uncracked conditions, code-based stiffness degradation, and beam-distributed cracking models using SAP2000. The results demonstrated that the modeling approach used to represent cracking significantly influences both global and local nonlinear structural behavior, particularly in terms of stiffness degradation patterns, plastic hinge development, modal characteristics, and energy dissipation mechanisms.

The findings indicate that the manner in which cracking is modeled plays a key role in governing the balance between global and local response characteristics. Uniform code-based stiffness reduction tends to induce more pronounced global softening and concentrated inelastic demand, whereas beam-distributed cracking provides a more gradual and spatially distributed representation of stiffness degradation, leading to a more balanced internal force redistribution and a more realistic simulation of flexural behavior in reinforced concrete beams.

From an engineering perspective, simplified uniform cracking approaches may lead to conservative estimations of seismic demand, while distributed cracking models can better capture the progressive development of nonlinear behavior in RC frames. Therefore, careful selection of cracking representation is essential for reliable seismic performance assessment of reinforced concrete structures.

The present study is subject to certain limitations that should be considered in interpreting the results. The analysis is performed on regular 3-, 6-, and 9-story reinforced concrete moment-resisting frames, and extension to irregular or taller structures requires further investigation. Only three near-fault ground motion records were used, which provide a limited dataset for capturing full record-to-record variability. The modeling primarily focuses on beam cracking effects, while other deterioration mechanisms such as column damage, shear failure, and bond-slip effects are not explicitly considered. Recent studies have shown that column shear degradation and confinement effects can significantly influence the seismic response of RC frames. It has been demonstrated that neglecting shear behavior may reduce the accuracy of nonlinear RC frame analysis [46], while ANN-based approaches have been developed for predicting the shear response of RC columns under axial loading conditions [47]. Furthermore, recent data-driven formulations have highlighted the significant role of confinement parameters and sectional characteristics in evaluating concrete column performance [48, 49]. Therefore, future studies should incorporate column shear degradation, confinement effects, and other interacting deterioration mechanisms into the proposed framework to achieve a more comprehensive seismic assessment of RC moment-resisting frames [50]. In addition, the proposed modeling approach has not been independently validated against experimental frame-level results or detailed numerical simulations. Therefore, the obtained results should be interpreted within the adopted modeling assumptions. Furthermore, the present study focuses on global response indicators, including roof displacement, base shear, bending moment, and energy dissipation. Interstory drift ratio and other local damage indicators were not explicitly evaluated and are recommended for future investigations to provide a more comprehensive seismic performance assessment.

Statements & declarations

Author contributions

Ehsan Abbasalipour: Conceptualization, Idea, Methodology, Investigation, Visualization, Writing - Original Draft, Formal analysis.

Mehdi Dehestani: Conceptualization, Methodology, Supervision, Project administration, Validation, Writing - Review & Editing.

Aref Hasanzadeh: Data curation, Methodology, Validation, Writing - Review & Editing.

Funding

The authors declare that no funds, grants, or other support were received during the preparation of this manuscript.

Data availability

The data presented in this study will be available upon request from the corresponding author.

Declarations

The authors declare no conflict of interest.

Appendix A. Supplementary relations and detailed moment-area formulations

A.1. Interior continuous beam

To compute the displacement, the moment–area method is employed, and due to symmetry, only half of the span is considered. The integration domain is divided into four segments, and the displacement relation is obtained from the first moment of area of the bending moment diagrams. The moment-area equation is expressed as Eq. A.1.

$$\bar{X}_1 = 0.5L - \frac{x_1 A_1}{A_1} = 0.5L - \frac{\int_0^{L_p} \frac{xM_1}{EI_{eq}} dx}{\int_0^{L_p} \frac{M_1}{EI_{eq}} dx} \tag{A.1a}$$

$$\bar{X}_2 = 0.5L - \frac{x_2 A_2}{A_2} = 0.5L - \frac{\int_{L_p}^{0.239L} \frac{xM_1}{EI} dx}{\int_{L_p}^{0.239L} \frac{M_1}{EI} dx} \tag{A.1b}$$

$$\bar{X}_3 = 0.354L - \frac{x_3 A_3}{A_3} = 0.354L - \frac{\int_{L_p}^{0} \frac{xM_2^4}{EI} dx}{\int_{L_p}^{0.354L-L_p} \frac{M_2}{EI} dx} \tag{A.1c}$$

$$\bar{X}_4 = 0.354L - \frac{x_4 A_4}{A_4} = 0.354L - \frac{\int_{0.354L-L_p}^{0.354L} \frac{xM_2}{EI_{eq}} dx}{\int_{0.354L-L_p}^{0.354L} \frac{M_2}{EI_{eq}} dx} \tag{A.1d}$$

The beam deflection with reduced stiffness is obtained from Eq. A.2.

$$\Delta_2 = -2\left[\frac{W}{EI_{eq}}\left(-0.2495LL_p^3 + 0.201L^2L_p^2 - 0.04495L^3L_p\right) + \frac{W}{EI}\left(0.0044L^4 + 0.2495LL_p^3 - 0.201L^2L_p^2 + 0.004495L^3L_p\right)\right] \tag{A.2}$$

By equating the two expressions, the equivalent flexural rigidity is obtained as Eq. A.3.

$$\frac{1}{EI_{eq}} = \frac{1}{EI} + \frac{1}{24\beta k_\theta L} \tag{A.3}$$

where $\beta = -0.2495\alpha^3 + 0.201\alpha^2 - 0.004495\alpha, \alpha = \frac{L_p}{L}$.

A.2. Side continuous beam

A.2.1. At 0.518L

Due to symmetry, half of the beam span is considered for moment-area calculations. At $0.14L$, the bending moment is zero; therefore, this point is included in the integration limits. Since the moment-area is evaluated with respect to the midspan while integration begins from the support, the centroid locations are defined as Eq. A.4.

$$\bar{X}_1 = 0.518L - \frac{\int_0^{L_p} \frac{M}{EI_{eq}} dx}{\int_0^{L_p} \frac{xM}{EI_{eq}} dx} \tag{A.4a}$$

$$\bar{X}_2 = 0.518L - \frac{\int_{L_p}^{0.14L} \frac{M}{EI} dx}{\int_{L_p}^{0.14L} \frac{xM}{EI} dx} \tag{A.4b}$$

$$\bar{X}_3 = 0.518L - \frac{x_3 A_3}{A_3} = 0.518L - \frac{\int_{0.14L}^{0.518L-L_P} \frac{M}{EI}\,dx}{\int_{L_P}^{0.354L-L_P} \frac{xM}{EI}\,dx} \tag{A.4c}$$

$$\bar{X}_4 = 0.518L - \frac{x_4 A_4}{A_4} = 0.518L - \frac{\int_{0.518L-L_P}^{0.518L} \frac{M_2^4}{(EI)_{eq}}\,dx}{\int_{0.518L-L_P}^{0.518L} \frac{xM_2}{(EI)_{eq}}\,dx} \tag{A.4d}$$

The beam deflection with reduced stiffness is given by Eq. A.5.

$$\Delta_2 = \frac{W}{EI_{eq}}\left(-0.1723LL_p^3 + 0.2016L^2L_p^2 - 0.0324L^3L_p\right) + \frac{W}{EI_1}\left(-0.003626L^4 + 0.1723LL_p^3 - 0.2016L^2L_p^2 + 0.0324L^3L_p\right) \tag{A.5}$$

By equating the expressions, the equivalent stiffness is obtained as Eq. A.6.

$$\frac{1}{EI_{1eq}} = \frac{1}{EI_1} + \frac{0.01506}{\beta_1 k_\theta L} \tag{A.6}$$

where $\beta_1 = 0.1663\alpha_1^3 - 0.1878\alpha_1^2 + 0.02913\alpha_1, \alpha_1 = \frac{L_p}{1.036L}$.

A.2.2. At 0.482L

For moment-area evaluation, half of the beam span is used due to symmetry. In addition, the integration domain is divided into four regions because of variations in bending moment expressions and stiffness along the span. The centroid locations are defined as in Eq. A.7.

$$\bar{X}_1 = 0.482L - \frac{\int_0^{L_P} \frac{M_2}{EI_2}dx}{\int_0^{L_P} \frac{xM_1}{EI_2}dx} \tag{A.7a}$$

$$\bar{X}_2 = 0.482L - \frac{\int_{L_P}^{0.242L} \frac{M_1}{EI_2}dx}{\int_{L_P}^{0.14L} \frac{xM_1}{EI_2}dx} \tag{A.7b}$$

$$\bar{X}_3 = 0.378L - \frac{\int_0^{0.378L-L_P} \frac{M_2}{EI_2}dx}{\int_0^{0.378L-L_P} \frac{xM_2}{EI_2}dx} \tag{A.7c}$$

$$\bar{X}_4 = 0.378L - \frac{\int_{0.378L-L_P}^{0.378L} \frac{M_2}{EI_2}dx}{\int_{0.378L-L_P}^{0.378L} \frac{xM_2}{EI_2}dx} \tag{A.7d}$$

The corresponding deflection expression is given by Eq. 14, and the reduced-stiffness form is expressed in Eq. A.8.

$$\Delta_2 = 2\left[\frac{W}{EI_{2eq}}\left(-0.2758LL_p^3 + 0.1016L^2L_p^2 + 0.1113L^3L_p + 0.21595L^4\right) + \frac{W}{EI_2}\left(-0.00256L^4 + 0.2758LL_p^3 - 0.10165L^2L_p^2 + 0.1113L^3L_p - 0.21595L^4\right)\right] \tag{A.8}$$

Finally, by equating the expressions, the equivalent stiffness is obtained as Eq. A.9.

$$\frac{1}{EI_{2eq}} = \frac{1+0.003095/\beta_2}{EI_2} + \frac{0.01041}{\beta_2 k_{\theta 2} L} \tag{A.9}$$

where $\beta_2 = 0.21595\alpha_2^4 - 0.2861\alpha_2^3 + 0.1094\alpha_2^2 + 0.1242\alpha_2, \alpha_2 = \frac{L_p}{0.964L}$.

References

[1] Chen, G., Baker, G., Hunt, G. W. Computational approach to localization using global energy minimization. Computers & Structures, 2000; 78: 529–536. doi:10.1016/S0045-7949(00)00043-2.

[2] Degroot, A. K., Kusters, G. M. A., Monnier, T. Concrete mechanics. Part B: Numerical modelling of bond slip behavior. Washington, D.C. (US): NASA; 1981. Report No.: 82.

[3] Eligehausen, R., Popov, E. P., Bertero, V. V. Local bond stress-slip relationships of deformed bars under generalized excitations: experimental results and analytical model. Berkeley (CA): University of California, Berkeley; 1983. Report No.: UCB/EERC-83/23.

[4] Kwak, H.-G., Filippou, F. Finite element analysis of reinforced concrete structures under monotonic loads. Berkeley (CA): University of California, Berkeley; 1990. Report No.: UCB/SEMM-90/14.

[5] Kwak, H.-G., Filippou, F. Finite element analysis of reinforced concrete structures under monotonic and cyclic loads. In: 10th World Conference in Earthquake Engineering; 1992 Jul 19–24; Madrid, Spain. p. 4227–4232.

[6] Kwak, H.-G., Filippou, F. A New Reinforcing Steel Model With Bond-Slip. Structural Engineering and Mechanics, 1995; 3: 299–312. doi:10.12989/sem.1995.3.4.299.

[7] Monti, G., Filippou, F., Spacone, E. Analysis of hysteretic behavior of anchored reinforcing bars. ACI Structural Journal, 1997; 94: 248–261. doi:10.14359/477

[8] Monti, G., Filippou Filip, C., Spacone, E. Finite Element for Anchored Bars under Cyclic Load Reversals. Journal of Structural Engineering, 1997; 123: 614–623. doi:10.1061/(ASCE)0733-9445(1997)123:5(614).

[9] Monti, G., Spacone, E. Reinforced Concrete Fiber Beam Element with Bond-Slip. Journal of Structural Engineering, 2000; 126: 654–661. doi:10.1061/(ASCE)0733-9445(2000)126:6(654).

[10] Spacone, E., Filippou, F. C., Taucer, F. F. Fibre Beam–Column Model For Non-Linear Analysis of R/C Frames: Part I. Formulation. Earthquake Engineering & Structural Dynamics, 1996; 25: 711–725. doi:10.1002/(SICI)1096-9845(199607)25:7<711::AID-EQE576>3.0.CO;2-9.

[11] Gan, Y. Bond stress and slip modeling in nonlinear finite element analysis of reinforced concrete structures [Master's Thesis]. Toronto (CA): University of Toronto; 2000.

[12] Lowes, L., Moehle, J., Govindjee, S. Concrete-steel bond model for use in finite element modeling of reinforced concrete structures. ACI Structural Journal, 2004; 101: 501–511. doi:10.14359/13336.

[13] Jendele, L., Cervenka, J. Finite element modelling of reinforcement with bond. Computers & Structures, 2006; 84: 1780–1791. doi:10.1016/j.compstruc.2006.04.010.

[14] Kwak, H.-G., Kim, J.-K. Implementation of bond-slip effect in analyses of RC frames under cyclic loads using layered section method. Engineering Structures, 2006; 28: 1715–1727. doi:10.1016/j.engstruct.2006.03.003.

[15] Beconcini, M. L., Croce, P., Formichi, P. Influence of bond-slip on the behaviour of reinforced concrete beam to column joints-Tailor Made Concrete Structures: New Solutions for our Society. In: International FIB Symposium; 2008 May 19–21; Amsterdam, Netherlands. p. 533–539.

[16] Zhou, Y. D., Cheuk, C. Y., Tham, L. G. An embedded bond-slip model for finite element modelling of soil–nail interaction. Computers and Geotechnics, 2009; 36: 1090–1097. doi:10.1016/j.compgeo.2009.03.002.

[17] Kwak, H.-G., Kim, S.-P. Simplified monotonic moment–curvature relation considering fixed-end rotation and axial force effect. Engineering Structures, 2010; 32: 69–79. doi:10.1016/j.engstruct.2009.08.017.

[18] Murcia-Delso, J., Stavridis, A., Shing, B. Modeling the bond-slip behavior of confined large-diameter reinforcing bars. In: 3rd International Conference on Computational Methods in Structural Dynamics and Earthquake Engineering, COMPDYN; 2011 May 25–28; Corfu, Greece. p. 1–14.

[19] Liang, X. An investigation of bond-slip behavior of reinforcing steel subjected to inelastic strains [Master's Thesis]. Ames (IA): Iowa State University; 2013.

[20] Coccia, S., Di Maggio, E., Rinaldi, Z. Bond slip model in cylindrical reinforced concrete elements confined with stirrups. International Journal of Advanced Structural Engineering (IJASE), 2015; 7: 365–375. doi:10.1007/s40091-015-0104-7.

[21] Shafaie, J., Hosseini, A., Marefat, M. 3D finite element modelling of bond-slip between rebar and concrete in pull-out test. In: 3rd International Conference on Concrete & Development, Iran; 2009 April 27; Tehran, Iran. doi:10.13140/2.1.2012.1605.

[22] Alijani, A., Khomami Abadi, M., Razzaghi, J. A new technique in the modal analysis of cracked reinforced concrete (RC) beams through the finite element method. Journal of Structural and Construction Engineering, 2020; 7: 5–30. doi:10.22065/JSCE.2018.127880.1535.

[23] Khademalrasoul, A. Simulation of the effect of internal heterogeneous linear and curved boundaries on crack propagation path in mixed mode using the level set method. Journal of Structural and Construction Engineering, 2017; 4: 42–54. doi:10.22065/jsce.2017.67302.1001.

[24] Hakimi, A., Moslemi, H. Modeling of Analysis Crack using Adaptive Finite Element Method Via Stress Intensity Factor Error Estimation. Journal of Structural and Construction Engineering, 2015; 2: 57–68.

[25] Dehghan Manshadi, S. M., Nategh, S., Khojasteh, A., Rahimian, M. Fracture Modes of an Annular Crack in a Transversely Isotropic Solid. Amirkabir Journal of Civil Engineering, 2018; 50: 855–864. doi:10.22060/ceej.2017.12713.5255.

[26] Miri, M., Rakhshanimehr, M., Miri, F. The effect of Cover, Pressure Strength, and bars corrosion on Cracking of Reinforced Concrete Structures. Amirkabir Journal of Civil Engineering, 2017; 49: 251–262. doi:10.22060/ceej.2016.693.

[27] Hajighasemali, S., Ramezanianpour, A. A., Kashefizadeh, M. Analytical Modeling of Load-Deflection Curve in Reinforced Concrete Beams. Amirkabir Journal of Civil Engineering, 2016; 47: 63–70. doi:10.22060/ceej.2016.614.

[28] Broujerdian, V., Sherafati, A., Karimpour, H. Effect of Crack Cohesive Stresses on the Load-Deformation Response of Reinforced Concrete Beams. Amirkabir Journal of Civil Engineering, 2018; 50: 89–96. doi:10.22060/ceej.2017.11366.5012.

[29] Okamura, H., Maekawa, K. Nonlinear Analysis and Constitutive Models of Reinforced Concrete. 1st ed. Tokyo (JP): Giho-do Press; 1991.

[30] Shima, H., Chou, L., Okamura, H. Micro and Macro Models for Bond Behavior in Reinforced Concrete. Journal of the Faculty of Engineering, Univ. of Tokyo, 1987; 39: 133–194.

[31] Maekawa, K., Okamura, H., Pimanmas, A. Non-Linear Mechanics of Reinforced Concrete. 1st ed. London (UK): CRC Press; 2003. doi:10.1201/9781482288087.

[32] Soltani, M., Maekawa, K. Path-dependent mechanical model for deformed reinforcing bars at RC interface under coupled cyclic shear and pullout tension. Engineering Structures, 2008; 30: 1079–1091. doi:10.1016/j.engstruct.2007.06.013.

[33] Birely, A. C., Lowes, L. N., Lehman, D. E. A model for the practical nonlinear analysis of reinforced-concrete frames including joint flexibility. Engineering Structures, 2012; 34: 455–465. doi:10.1016/j.engstruct.2011.09.003.

[34] Vandecruys, E., Hendriks, M. A. N., van de Velde, M., Lombaert, G., Verstrynge, E. Dynamic stiffness parameter assessment of cracked reinforced concrete beams: A numerical and experimental study. Engineering Structures, 2024; 318: 118758. doi:10.1016/j.engstruct.2024.118758.

[35] Kordtabar, B., Dehestani, M., Yazdanpanah, O., Hasanzadeh, A. Time-dependent seismic fragility and serviceability assessment of reinforced concrete frames under chloride-induced corrosion. Scientific Reports, 2025; 15: 40575. doi:10.1038/s41598-025-24197-z.

[36] Zhang, H. Y., Li, Q. Y., Kodur, V., Lv, H. R. Effect of cracking and residual deformation on behavior of concrete beams with different scales under fire exposure. Engineering Structures, 2021; 245: 112886. doi:10.1016/j.engstruct.2021.112886.

[37] Dancygier, A. N., Karinski, Y. S. Effect of cracking localization on the structural ductility of normal strength and high strength reinforced concrete beams with steel fibers. International Journal of Protective Structures, 2019; 10: 457–469. doi:10.1177/2041419618824609.

[38] Namdar, A., Darvishi, E., Feng, X., Zakaria, I., Mat Yahaya, F. Effect of flexural crack on plain concrete beam failure mechanism: A numerical simulation. Fracture and Structural Integrity, 2016; 10: 168–181. doi:10.3221/IGF-ESIS.36.17.

[39] Karinski, Y. S., Dancygier, A. N., Gebreyesus, Y. Y. Probabilistic model for cracking localization in reinforced fibrous concrete beams. Journal of Engineering Mathematics, 2024; 144: 23. doi:10.1007/s10665-023-10330-2.

[40] Fu, C., Zhu, Y., Tong, D. Stiffness Assessment of Cracked Reinforced Concrete Beams Based on a Fictitious Crack Model. KSCE Journal of Civil Engineering, 2021; 25: 516–528. doi:10.1007/s12205-020-2056-0.

[41] Forouzan, S. Effect of bond-slip on the ductility of reinforced concrete beams [Thesis]. Babol (IR): Babol Noshirvani University of Technology; 2016.

[42] Ayoub, A., Filippou Filip, C. Mixed Formulation of Bond-Slip Problems under Cyclic Loads. Journal of Structural Engineering, 1999; 125: 661–671. doi:10.1061/(ASCE)0733-9445(1999)125:6(661).

[43] Gergely, P., Lutz, L. A. Maximum Crack Width in Reinforced Concrete Flexural Members. 318Reference, 2005; 10: 87–117. doi:10.14359/17348.

[44] Bayrak, O., Sheikh, S. High-strength concrete columns under simulated earthquake loading. 1997; 94: 708–722.

[45] PEER ground motion database. Pacific Earthquake Engineering Research Center. 2010. Available online: https://ngawest2.berkeley.edu/. (Accessed December 2010).

[46] Shayanfar, J., Akbarzadeh Bengar, H. Nonlinear analysis of RC frames considering shear behaviour of members under varying axial load. Bulletin of Earthquake Engineering, 2017; 15: 2055–2078. doi:10.1007/s10518-016-0060-z.

[47] Sadeghpour Haji, M., Niknam, R., Shayanfar, J. ANN-Based Modeling of Shear Behavior of Reinforced Concrete Columns under Constant Axial Loads. Civil Engineering and Applied Solutions, 2026; 2: 28–48. doi:10.22080/ceas.2025.30228.1050.

[48] Shayanfar, S., Ghasemi Naghibdehi, M., Shayanfar, J. Data-Driven Prediction of FRP Confinement Efficiency in Concrete Columns: Incorporating Corner Radius and Aspect Ratio Effects. Civil Engineering and Applied Solutions, 2026; 2: 1–15. doi:10.22080/ceas.2026.30750.1059.

[49] Shayanfar, S., Ghasemi Naghibdehi, M., Shayanfar, J. Data-Driven Predictive Formulation for FRP-Confined Circular Concrete Columns. Civil Engineering and Applied Solutions, 2027; 3: 25–36. doi:10.22080/ceas.2026.30751.1060.

[50] Javad, S., Meysam, O., Mahdi, N. Analysis-oriented model for seismic assessment of RC jacket retrofitted columns. Steel and Composite Structures, An International Journal, 2020; 37: 371–390. doi:10.12989/scs.2020.37.3.371.